

Electrically and optically active charge carrier traps in silicon-doped few-layer GaSe

M. Bissolo,^{1,*)} R. Li,^{1,†)} M. Ogura,² Z. Sofer,³ S. Polesya,² D. Han,⁴ A. W. Holleitner,¹ C. Kastl,¹ G. Koblmüller,^{1,5} H. Ebert,² E. Zallo,^{1,‡)} and J. J. Finley¹

¹⁾Walter-Schottky-Institut and TUM School of Natural Sciences, Technische Universität München, Am Coulombwall 4, 85748 Garching, Germany

²⁾Department of Chemistry, Ludwig-Maximilians-Universität München, Butenandtstrasse 5-13, 81377 München, Germany

³⁾Department of Inorganic Chemistry, University of Chemistry and Technology Prague, Technická 5, 166 28 Prague 6, Czech Republic

⁴⁾School of Materials Science and Engineering, Jilin University, Changchun, 130012 China

⁵⁾Institute of Physics and Astronomy, Technical University Berlin, Hardenbergstrasse 36, 10623 Berlin, Germany

(Dated: 5 February 2026)

Understanding defects in atomically thin van der Waals (vdW) semiconductors is essential for advancing their use in next-generation optoelectronic and photovoltaic devices. Here, we apply a combination of various impedance spectroscopy techniques to two-dimensional (2D) vdW GaSe doped with silicon (Si) to reconstruct deep trap states across the full bandgap. Deep-level transient spectroscopy reveals three distinct deep states 0.31, 0.88, and 1.40 eV below the conduction band edge. Complementary deep-level optical spectroscopy and photocapacitance measurements identify three deep states at 1.4 and 1.8 eV below the conduction band edge, and 2.0 eV above the valence band edge, with thermal admittance spectroscopy providing additional verification and further resolving two trap states, at 0.16 eV above the valence band edge and at 0.26 eV below the conduction band edge. By comparing the experimentally extracted ionization energies with the predictions of density functional theory, our results attribute these trap states primarily to Si-related defects and metal vacancies. This work presents a comprehensive defect map of Si-doped GaSe, providing critical insights into carrier trapping mechanisms that are essential for optimizing the design of 2D material-based devices for industrial applications.

I. INTRODUCTION

The performance of semiconductor-based (opto)electronic devices is very strongly influenced by deep levels that act as charge traps or recombination centers. These defects, while potentially detrimental to device efficiency, can also serve as functional components in emerging technologies. For example, deep levels can enhance the catalytic activity of 2D materials for the hydrogen evolution reaction, but also operate as spin-active color centers with potential for applications in spin–photon interfaces or for quantum metrology^{1–4}. As the field of two-dimensional (2D) van der Waals (vdW) materials continues to expand, understanding and characterizing electrically active mid-gap defects within this class of semiconductors has become crucial for the advancement of 2D-based devices. Among the diverse 2D vdW materials, the post-transition metal monochalcogenide (PTMC) GaSe⁵ has garnered significant attention due to its promising electronic and optoelectronic properties. GaSe transistors exhibit high on/off current ratios, exceptional photoresponse, and promising (photo)electrochemical capabilities^{5–9}, making the materials system attractive for next-generation technologies.

Few-layer GaSe is of particular interest since its valence band lies at the transition between a conventional parabolic

dispersion and a caldera-like, ring-shaped dispersion, yielding near-flat bands and a van Hove singularity at the valence band maximum (VBM)^{10–12}. These result in a low carrier group velocity and a strongly enhanced density of states (DOS), which amplifies many-body interactions such as excitonic or correlation effects. These same electronic features, combined with the intrinsically low thermal conductivity, also lead to enhanced Seebeck coefficients, higher power factors, and improved thermoelectric performance^{13,14}. For example, theoretical calculations of a GaSe/SnS₂ van der Waals heterostructure predict very high thermoelectric performance, with a figure of merit zT reaching 2.99 at 700 K for n-doped GaSe¹⁵. However, the nature of the PTMC band structure also makes these materials highly sensitive to disorder: even weak defect potentials can strongly modify carrier transport, thereby degrading mobility, optical response, and thermoelectric performance^{16,17}.

Realizing specifically doped GaSe devices, or complementary p-n junctions for photovoltaics, LEDs, and photocatalytic applications, requires reliable n- and p-type doping. However, achieving such doping in atomically thin materials is notoriously challenging due to their high surface-to-volume ratio and their strong sensitivity to structural damage. In conventional III–V semiconductors such as gallium arsenide, silicon can incorporate on both cation and anion sites, acting either as a donor or an acceptor depending on its lattice position^{18–21}. This amphoteric behaviour can lead to compensation effects, underscoring the importance of understanding dopant-related defects. In contrast, for GaSe, studies on Si incorporation and its associated defect configurations remain scarce, and under-

^{*}michele.bissolo@tum.de

[†]Current address: Max Planck Institute for Chemical Physics of Solids, Nöthnitzer Str. 40, 01187 Dresden, Germany

[‡]eugenio.zallo@tum.de

standing these dopant-induced defects is essential for assessing their impact on carrier dynamics and device performance.

Defect characterization in semiconducting 2D materials relies on techniques with varying trade-offs. Photoluminescence, Raman and X-ray photoemission spectroscopies are non-invasive and device-compatible but often provide only qualitative or indirect information^{22–24}. Scanning tunneling and transmission electron microscopies offer atomic resolution but require complex sample preparation and can be destructive^{25,26}. In contrast, capacitance-based spectroscopic techniques, such as Deep Level Transient Spectroscopy (DLTS), are a highly sensitive and non-destructive approach to probing electrically active states. DLTS has proven its utility in bulk²⁷ and single-layer²⁸ transition metal dichalcogenide semiconductors by providing quantitative information on energy levels and capture cross-sections. However, shallow traps and minority carrier bands have not been accessible. Similarly, Deep Level Optical Spectroscopy (DLOS) is a powerful and quantitative approach to accessing deep-level defect states across a wide energy range^{29,30}, enabling the investigation of traps near both band edges.

In this study, we employ a combination of impedance spectroscopy techniques, including DLTS, DLOS, and temperature- and frequency-dependent capacitance-voltage profiling, to investigate defect states in exfoliated Si-doped few-layer GaSe. By systematically exciting GaSe electrically and optically, we reconstruct a comprehensive picture of electrically active defect states within the GaSe bandgap. The experimentally derived trap ionisation energies are then compared with density functional theory (DFT) calculations to identify the specific defects responsible for the observed states. These insights not only elucidate the defect landscape of silicon-doped GaSe and its impact on carrier dynamics but also establish a robust framework for defect characterization in other doped 2D vdW semiconductors.

II. RESULTS

Modulation of trap occupancy in monolayer 2D semiconductors is challenging due to the atomic-scale thickness, which prevents the formation of a significant vertical depletion width in a Schottky diode, the conventional device geometry for DLTS measurements. By contrast, a metal-insulator-semiconductor (MIS) structure allows for the tuning of the surface Fermi level via a back-gate voltage, enabling the filling and emptying of defects over a wider range of biases. Studies on monolayer MoS₂ show DLTS in MIS geometries where trap filling is gate-modulated, overcoming the limitations of vertical Schottky devices²⁸. Moreover, using hBN as the insulator in MIS structures reduces interface state densities substantially due to its atomic flatness and van der Waals bonding³¹. Based on this, we prepared the GaSe-based MIS capacitor as depicted in Figure 1a. The device stack consists of a rectangular Pt (7 nm) top gate, a 15 nm hBN dielectric, a 7.1 nm GaSe layer, and a thin graphite bottom contact running across the GaSe to achieve a more homogeneous potential distribution. The vdW heterostructure

is assembled using a PDMS/PC stamp (propylene carbonate film on polydimethylsiloxane), which is then aligned and transferred onto a sapphire substrate. Afterwards, the Pt gate and electrical contacts are defined and evaporated on top. The sapphire substrate is advantageous for suppressing background-related charges, thereby minimizing parasitic effects, and reducing electrical noise arising from capacitive coupling. The doping of GaSe was confirmed by secondary ion mass spectrometry (SIMS), which revealed a Si concentration of $\sim 10^{20} \text{ cm}^{-3}$ (see Figure S1 in the Supplementary Information). Figure 1b shows typical room-temperature CV curves recorded at 500 Hz and 700 kHz, by sweeping the back-gate voltage from -8.5 V to $+6 \text{ V}$ and back, while applying a 50 mV AC signal. At low frequencies, leakage currents restricted the usable gate voltage range to -8 V to $+5 \text{ V}$, whereas this effect was suppressed at higher frequencies. As expected for MIS devices, three operating modes can be distinguished in the profile, such as inversion, depletion, and accumulation³². The strong gate-voltage dependence of the capacitance confirms the efficient Fermi-level modulation, and the absence of noticeable frequency dispersion in the strong accumulation regime indicates low series resistance at the contacts. From the CV response, the device clearly exhibits n-type behaviour, consistent with the successful Si incorporation into the GaSe lattice³³. The inversion capacitance is suppressed at high frequencies, as expected, since minority carriers cannot be generated or transported quickly enough to follow the AC modulation. The forward and backward hysteresis, measured at room temperature at half of the geometric capacitance in the weak accumulation regime, is 0.73 and 0.08 V for 500 Hz and 700 kHz, respectively (0.10 and 0.03 V at 70 K), indicating a low density of long-lived traps. In the following sections, further frequency- and temperature-dependent studies will be discussed to extract trap signatures and quantify defect-related states.

DLTS measurements on a few-layer GaSe MIS device were performed at the onset of the accumulation regime. The populating voltage pulse of 25 ms was set to 4.6 V, and the transients were recorded at 3.8 V. Figure 1c shows the heatmap of the DLTS signal constructed from the temperature-dependent capacitance transients (see the Supplementary Information for details on optimization of the measurement and the algorithm used for signal extraction). Each feature in the DLTS signal corresponds to the lifetime of specific mid-gap states as a function of temperature. The emission rate e_n of an electron deep-level state follows the expression³⁴:

$$e_n = \sigma_n v_{\text{th},n} N_C \exp\left(-\frac{\Delta E}{kT}\right), \quad (1)$$

where σ_n is the capture cross-section, $v_{\text{th},n} = \sqrt{\frac{2k_B T}{m^*}}$ the thermal velocity of electrons in 2D, $N_C = \frac{8\pi m^* k_B T}{h^2}$ the effective density of states in the 2D conduction band, ΔE the activation energy of the trap, k is the Boltzmann constant, and T the absolute temperature (see Supplementary Information for further details). An analogous expression holds for hole

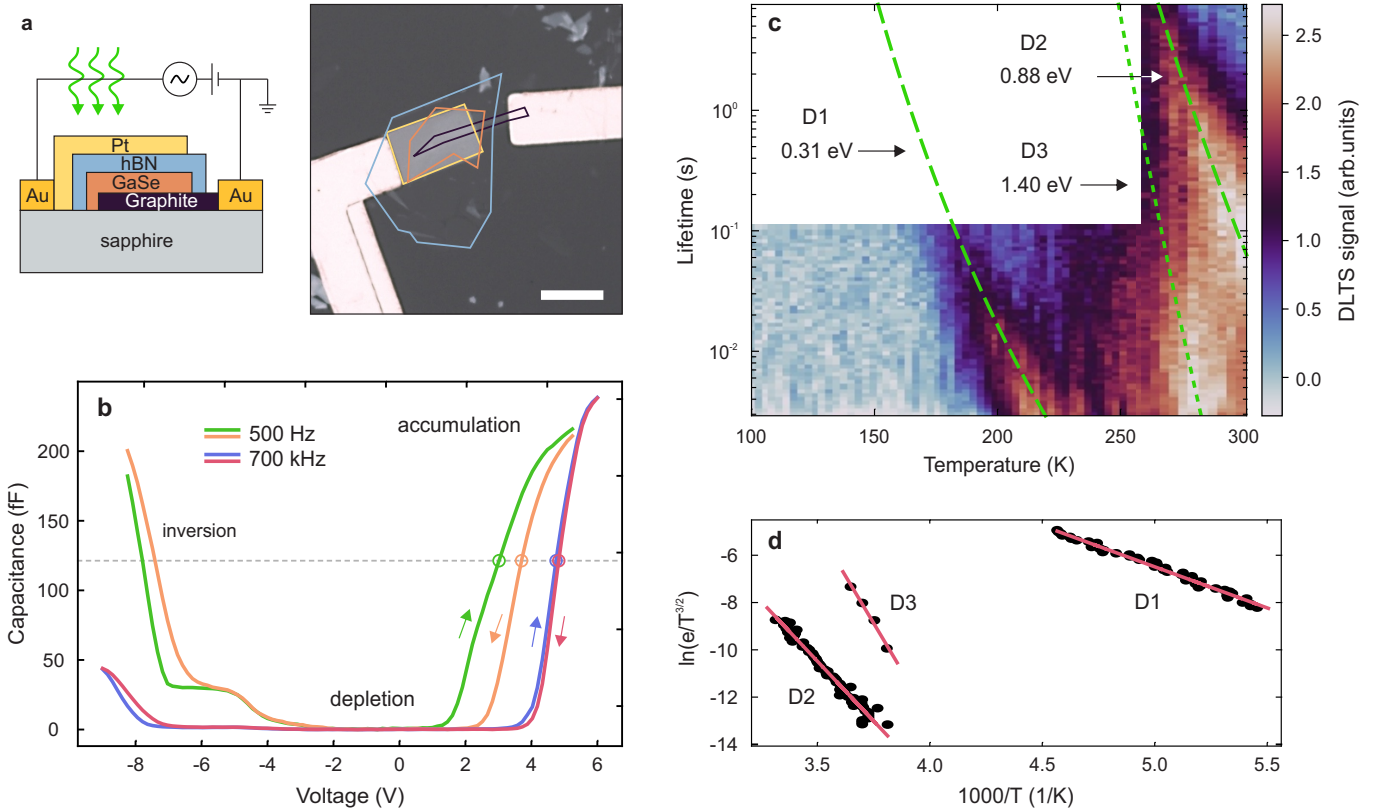


FIG. 1. (a) Schematic (left) and optical micrograph (right) of the GaSe metal-insulator-semiconductor (MIS) device (left). (b) Forward and backward CV sweeps at 500 Hz and 700 kHz (room temperature). The grey dotted line indicates the position of half the geometric capacitance. (c) Heat map of the DLTS measurement for temperatures ranging between 100 K and 300 K and (d) Arrhenius plot (black points) of the temperature-dependent lifetime of the identified defects with respective fits (red lines). The dashed green lines in (c) are computed from the Arrhenius fits in (d). To limit measurement duration, temperatures below 257 K were limited to measured lifetimes of a maximum of 100 ms.

emission. The activation energies and capture cross-sections of the identified defect states can be determined using a linear fit to the Arrhenius plot after extracting the maxima positions of the DLTS signal for each feature (Figure 1d). The DLTS analysis reveals three distinct defect energy levels at 0.31 ± 0.01 eV (D1), 0.88 ± 0.02 eV (D2) and 1.40 ± 0.12 eV (D3) below the conduction band minimum (CBM, E_c). By assuming a 2D thermal velocity, an effective electron density of states²⁸ (see Supplementary Information), and employing an in-plane electron effective mass $m_n = 0.2m_0$ ^{35,36}, we determine a capture cross-section for D1 of $(7.16 \pm 2.51) \times 10^{-17}$ cm, consistent with a point defect. The capture cross sections of D2 and D3 could not be extracted due to a large fit error. Note that in the 2D formalism²⁸ the capture cross section has units of cm rather than cm^2 .

To investigate deep levels near the VBM and construct a clearer picture of the defect landscape, we used DLOS with monochromatic photons with energies ~ 1.3 to 2.6 eV. DLOS replaces the temperature sweep with an optical source, allowing the detrapping process to be driven by light. This enables probing a broader range of defect states across the band gap, depending on the wavelength used (see

Figure S2 and Note S2). Since the measurement records capacitance transients during optical excitation after all defects have been filled with electrons via a voltage pulse, it exclusively probes electron emission from traps relative to the CBM, without contributions from trap-to-trap transitions or optically-driven metastable charge capture by defects. The DLOS spectrum is shown in Figure 2a. The data was fitted with two curves based on Lucovsky's model³⁷ for localized traps, which assumes no lattice relaxation (i.e., neglects the Franck-Condon relaxation energy), and an Urbach-like exponential distribution of traps close to the VBM and CBM. The best fit is characterized by two trap states below the CBM at 1.38 ± 0.02 eV and 1.84 ± 0.01 eV, respectively. The signal increases up to the band edge of few-layer GaSe at 2.16 eV, after which the contribution from band-to-band transitions dominates the spectrum. The exponential fit of the signal close to the band-edge returns an Urbach energy of 63.10 ± 4.90 meV. To validate the DLOS results, we also performed steady-state photocapacitance (SSPC) measurements (see Figure 2b), which record the total capacitance change under monochromatic illumination once steady-state conditions are established. Since the steady-state signal reflects a dynamic equilibrium between

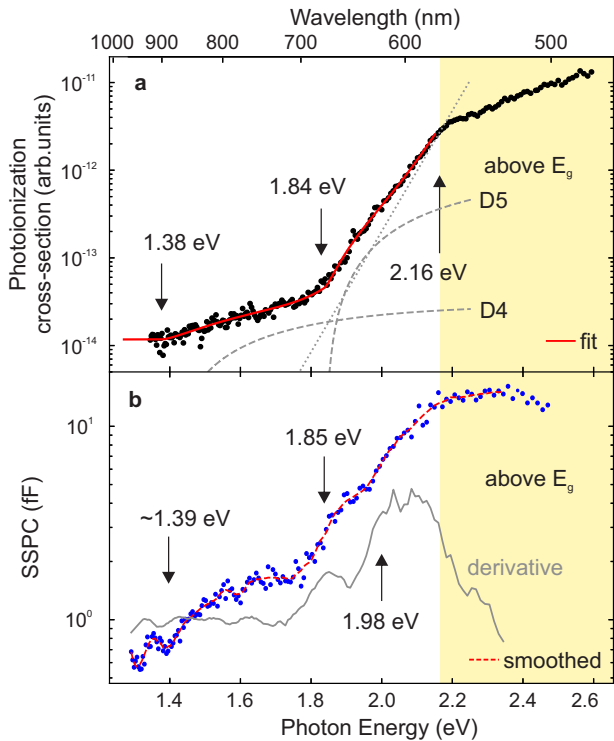


FIG. 2. (a) Deep Level Optical Spectroscopy (DLOS) and (b) steady-state photocapacitance (SSPC) of the GaSe MIS device. The black dashed lines in (a) show the fitting results using Lucosky's model. The gray line in (b) represents the derivative function used to determine the transitions.

photo-excitation (detrapping) and optically-driven recapture (retrapping) processes, the measured capacitance corresponds to the net trap occupancy. A step in the SSPC as a function of excitation energy indicates the activation of a new defect state. SSPC spectroscopy confirms the states close to 1.39 eV and 1.85 eV below the CBM observed in DLOS. The constant slope (see the gray curve in Figure 2b) close to the band edge is consistent with an increasing share of defects being excited, compatible with the Urbach-tail seen in the DLOS measurement. An additional feature not evident in the DLOS spectrum appears at 1.98 eV. This discrepancy arises because, as previously mentioned, under the present initialization and transient readout, DLOS selectively probes photo-emission of electrons from pre-filled traps into the conduction band, while SSPC, operating in steady state, also probes charge transfer between traps or from the valence band to traps. We therefore attribute the observed kink at 1.98 eV to a defect state located 0.18 eV below the CBM. Finally, both DLOS and SSPC spectroscopy consistently determine a bandgap of 2.16 eV, in agreement with reported values for GaSe^{11,38,39}.

We continue to investigate the temperature and frequency dependence of the capacitance-voltage (CV) characteristics in detail to probe the dynamic behaviour of the defects. Figure 3a shows the room-temperature CV curves, measured from -8.5 to 6 V, for a range of frequencies from 20 Hz to 700 kHz. A pronounced frequency dispersion is observed in

the weak accumulation regime, which cannot be attributed to series resistance effects, as the strong accumulation regime exhibits negligible frequency dispersion⁴⁰. Furthermore, a clear capacitance peak emerges at negative gate voltages but weakens and eventually vanishes as the measurement frequency increases. This is a characteristic signature of trap states with emission rates that are too slow to follow the AC probing signal at higher frequencies^{41,42}.

To elucidate the origin of these trap states, temperature-dependent CV measurements were carried out. Since the emission rate of trap states is thermally activated, changing the temperature shifts the frequency at which these states can respond, resulting in an Arrhenius-type dependence of the cut-off frequency. Figure 3b presents a false color image of the temperature-dependent CV curves measured at 500 Hz. The capacitance peak at negative voltages vanishes below a certain temperature (~ 175 K), consistent with the expected behaviour of discrete trap states whose emission rates fall below the probing frequency. In contrast, the dispersion observed at positive gate voltages does not disappear at a single temperature but rather diminishes gradually over a range of temperatures, depending on the applied bias. This behaviour indicates the presence of a distribution of defect states across a range of energies within the bandgap, such as those associated with an Urbach tail. It is important to note that the onset of accumulation occurs at lower gate voltages for higher temperatures.

To further investigate the origin of the frequency-dependent capacitance features and understand the role of minority carriers in the trap emission rates, Thermal Admittance Spectroscopy (TAS) measurements⁴³ were performed under different gate bias conditions. TAS yields defect energy levels and capture cross-sections by tracking the demarcation AC frequency, ω_0 , at which a given defect feature vanishes as temperature changes (see Supplementary Information for details). As the temperature decreases, the defect emission rate, $1/\tau(T)$, falls toward the probing frequency, ω_{ac} . In the limit that

$$\omega_0(T) = \frac{1}{\tau(T)} < \omega_{ac},$$

the defect can no longer respond to the AC modulation and ceases to contribute to the total capacitance. By identifying the temperature at which each feature disappears, we reconstruct the temperature dependence of the defect lifetime. An Arrhenius analysis of $\omega_0(T)$ then allows extraction of the defect activation energy and capture cross-section, in direct analogy to the DLTS procedure (see Figure 1c,d). Importantly, both the inversion capacitance and the capacitance peak disappear simultaneously as either the temperature is lowered or the probing frequency is increased, indicating a common, kinetically limited origin. This behavior is consistent with a trap-mediated, thermally activated emission process that supplies minority carriers to the inversion charge. We exclude a diffusion-limited minority-carrier response, as no systematic dependence of the cutoff frequency on gate voltage is observed. In a diffusion-limited scenario, the characteristic response time would scale with the depletion width and therefore vary with bias. The absence of such a trend

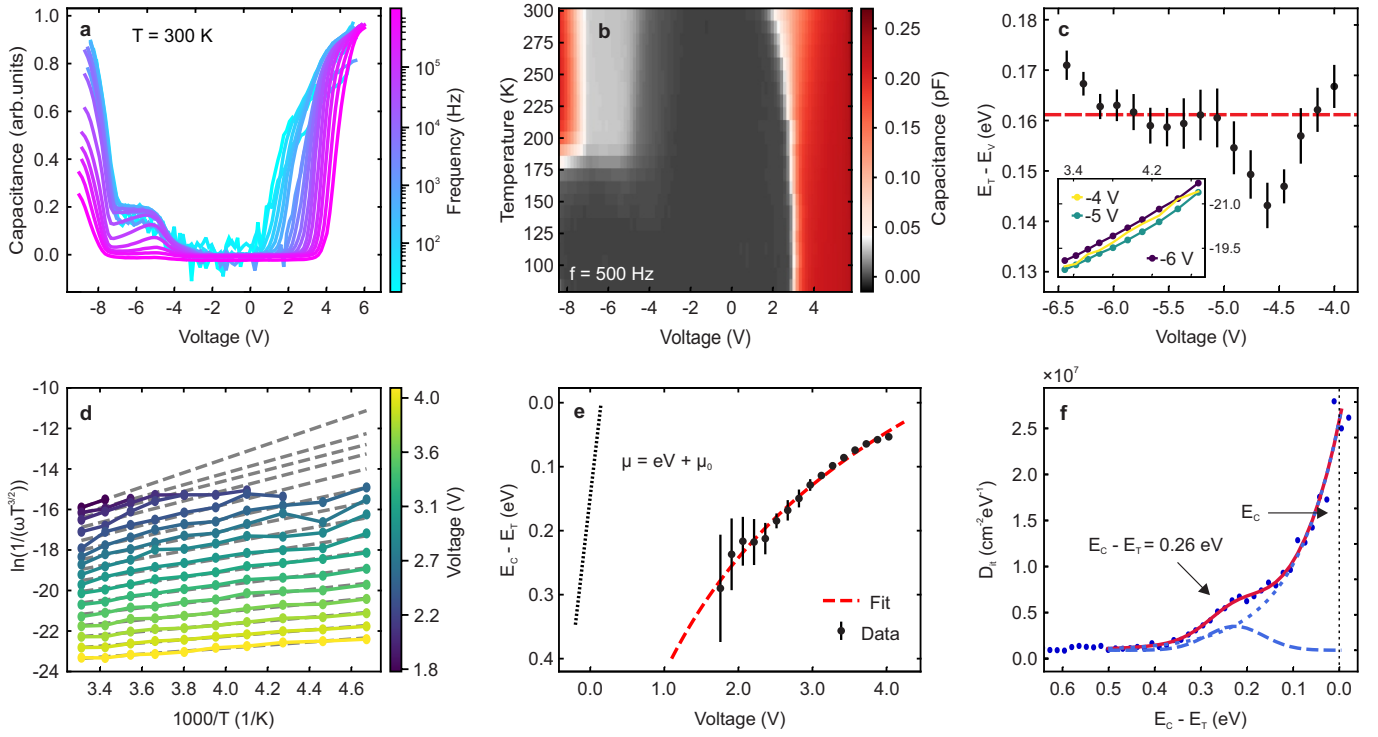


FIG. 3. (a) CV measurements taken at frequencies ranging from 20 Hz to 700 kHz. (b) Temperature-dependent CV profiling at 500 Hz. (c) Acceptor energy as a function of voltage, as extracted from the Thermal Admittance Spectroscopy (TAS) measurement in the inversion regime. The inset shows the Arrhenius plot of the detrapping lifetime for -4, -5, and -6 V, plotted as $1000/T$ vs. $\ln(1/\omega T^{3/2})$. (d) Arrhenius plots of the detrapping lifetime at various voltages in the accumulation regime. (e) Acceptor energy as a function of voltage, as extracted from (d). The dashed red line is a fit of the voltage-dependent chemical potential $\mu(V)$. The dotted black line indicates $\mu(V)$ for a semiconductor with no gap states. (f) Defect density close to the conduction band. The energy position ($\mu(V)$) is computed from the fit in (e). The red line is a fit using the sum of an exponential function and a Gaussian.

instead supports an emission-limited Shockley–Read–Hall process, whose rate is governed by the defect activation energy and capture cross-section.

Figure 3c presents the trap energy, $E_T - E_v$, as a function of various negative gate voltages. We identify a trap level located at 0.16 ± 0.02 eV above VBM, with a large corresponding capture cross-section of $(2.41 \pm 1.24) \times 10^{-6}$ cm (see Supplementary Information for the derivation). Note that for 7.1 nm thick GaSe (8 monolayers), the valence band evolves from a parabolic shape to a caldera-like, ring-shaped structure, coinciding with the emergence of flat bands and a van Hove singularity near the VBM^{10,11}. The trap energy and capture cross-section values reported here are based on the implicit assumption of parabolic bands. As such, they are expected to represent effective values that may deviate significantly from their actual values. Notably, the capture cross-section should be interpreted with care, since it neglects the effects of low group velocity and high density of states near the van Hove singularity, as well as the non-parabolic character of the effective hole mass ($m_p = -1.9m_0$)⁴⁴.

The same analysis was applied to the weak-accumulation regime. Figure 3d shows the Arrhenius plots of the demarcation frequency, ω_0 , for different gate voltages, and Figure 3e

displays the resulting trap energy relative to the CBM. We observe that, as the gate voltage increases, the extracted trap energy shifts closer to the CBM, consistent with a continuum of band-tail states. Consequently, raising the chemical potential enables probing of traps at progressively higher energies, providing an indirect measure of the chemical potential as a function of the applied voltage.

By assuming an exponential band-tail DOS we obtain for the voltage dependence of the chemical potential μ ,

$$V = \frac{\mu - \mu_0}{e} + \frac{eD_0E_0}{C_{\text{geom}}} \exp\left(\frac{\mu}{E_0}\right),$$

where μ_0 is the chemical potential at 0 V, e the elementary charge, D_0 and E_0 the amplitude and characteristic energy of the exponential band-tail, and C_{geom} the geometric capacitance (see Note S4 in the Supplementary Information). The dashed red line in Figure 3e shows the fit to this model, while the dotted black line represents the ideal $\mu(V)$ for a gap without band-tail states. From the fit, we extract a charge-neutrality Fermi level position of $\mu_0 = -0.79 \pm 0.29$ eV relative to the CBM and an Urbach characteristic energy $E_0 = 0.27 \pm 0.09$ eV.

Finally, the interface trap density, $D_{it}(V)$, is computed from the measured low- and high-frequency capacitances, $C_{lf}(V)$

and $C_{\text{hf}}(V)^{41,42}$, using

$$D_{\text{it}} = \frac{1}{q} \left[\frac{C_{\text{geom}} C_{\text{lf}}}{C_{\text{geom}} - C_{\text{lf}}} - \frac{C_{\text{geom}} C_{\text{hf}}}{C_{\text{geom}} - C_{\text{hf}}} \right].$$

By mapping V to energy through the relation for $\mu(V)$ introduced above, we plot $D_{\text{it}}(E)$ in Figure 3f. The trap distribution is well described by the sum of an exponential tail (Urbach-like) with a characteristic energy of 0.10 ± 0.01 eV and a Gaussian peak centered at 0.26 ± 0.02 eV, indicating a discrete electron trap superimposed on a band-tail background. These values are in reasonable agreement with the fit in Fig. 3e, with the remaining difference ascribed to the assumption of 0 K and the omission of the Gaussian peak contribution in the first fit, which, when neglected, artificially broaden the exponential tail.

Our results demonstrate that few-layer GaSe doped with Si hosts multiple energy levels within the band gap. DLTS measurements identified defect states at 0.31 eV, 0.88 eV, and 1.40 eV below the CBM, while TAS revealed a trap at 0.16 eV above the VBM and an Urbach-like band-tail density of states near the CBM, together with a another trap at 0.26 eV below the CBM. Optical techniques, including DLOS and SSPC, detected defect levels at 1.4 and 1.8 eV below the CBM, an additional transition at 1.98 eV above the VBM, and the bandgap at 2.16 eV. While these measurements provide a comprehensive experimental picture of the defect landscape in our materials, they do not yet clarify the microscopic origin of the observed states. Moreover, the influence of silicon doping on these defects remains largely unexplored in the literature. To address these open questions, we performed *ab initio* calculations using density functional theory (DFT) with the HSE06 hybrid functional (see Theoretical Methods in Section V). These calculations focused on a range of point defects, including gallium and selenium vacancies, oxygen-passivated vacancies, and silicon-related substitutional or interstitial defects. A summary of the calculated defect energy levels is presented in Table I and Figure 4.

TABLE I. Calculated defect transition levels relative to band edges.

	This work	Literature ⁴⁵
Charge transition level	2.02 eV	2.26 eV
$\text{Ga}_i(+/0)$	$E_C - 0.39$	$E_C - 0.2$
$\text{V}_{\text{Se}}(-/2-)$	–	$E_V + 1.6$
$\text{V}_{\text{Se}}(0/-)$	$E_V + 1.61$	$E_V + 1.1$
$\text{Ga}_{\text{Se}}(0/-)$	$E_V + 0.45$	–
$\text{Se}_{\text{Ga}}(0/-)$	$E_V + 0.25$	–
$\text{V}_{\text{Ga}}(0/-)$	$E_V + 0.04$	$E_V + 0.1$
Se_i	inactive	inactive
$\text{Si}_{\text{Ga}}(+/0)$	$E_C - 0.39$	$E_C - 0.7$
$\text{Si}_i(0/-)$	$E_V + 1.63$	–
$\text{Si}_{\text{Se}}(0/-)$	$E_V + 1.20$	–
$\text{O}_{\text{Ga}}(0/-)$	$E_V + 0.17$	–
O_{Se}	inactive	–
O_i	inactive	–

Figure 4 highlights the overall good agreement between our DFT calculations and the defect levels observed experimen-

tally, confirming the correspondence between theoretical predictions and DLTS measurements. In particular, the defect levels detected in DLTS align well with those predicted for silicon-related defects. It should be noted that the calculations were performed for bulk GaSe, leading to deviations of up to 0.14 eV (see Figures S4 and S5 in the Supplementary Information) from the experimental values. These deviations are ascribed to confinement-induced changes in the band structure of few-layer GaSe and also the use of plain DFT. Interestingly, the calculations indicate that oxygen-passivated selenium vacancies and interstitial oxygen atoms are electrically inactive.

III. DISCUSSION

A defect level at approximately 0.2 eV above the VBM has been consistently reported in GaSe across multiple studies, regardless of the doping type^{46–53}. This defect is commonly attributed to Ga vacancies, which act as acceptor levels. Structural studies using annular dark field-scanning transmission electron microscopy imaging have shown that Ga vacancies are indeed one of the predominant defects in atomically thin GaSe⁵⁴. Our TAS measurements reveal a defect level at 0.16 eV above the VBM, in good agreement with the reported values for Ga vacancies. However, this is in contrast with the theoretically obtained values, placing the defect transition level of V_{Ga} at 0.04 eV above the VBM (see Table I). The energy calculated by DFT for Si-based defects is in good agreement with our DLTS and TAS results. The experimentally observed defect levels at 0.31 and 0.88 eV (DLTS), and 0.26 eV (TAS) below the CBM, as well as 1.98 eV (SSPC) above the VBM (which corresponds to a shallow level 0.18 eV below the CBM given the 2.16 eV bandgap), are compatible with Si_{Ga} and Si_i (both predicted at 0.39 eV below the CBM), which act as an acceptor and donor, respectively, and with Si_{Se} (predicted at 0.82 eV), which act as an acceptor. However, the applied experimental techniques do not allow unambiguous determination of whether Si occupies Ga sites, interstitial positions, or both. The small offset between the DLTS/TAS and SSPC values is tentatively ascribed to the contribution of a small Franck-Condon relaxation energy, which causes the optical SSPC transition to appear at higher energy than the adiabatic charge-transition level measured by DLTS and TAS³⁰. To assess the likelihood of formation for the different Si-based defects, we computed their formation energy (see Figure S8 in the Supplementary Information) and we found that Si_i exhibits a considerably higher formation energy. In contrast, Si_{Ga} and Si_{Se} have comparable and lower formation energies, enabling us to exclude Si_i and assign the observed defect levels to Si_{Ga} and Si_{Se} . It is worth noting that according to our calculations, interstitial Ga introduces a donor gap state at the same energy as Si_{Ga} and Si_i . Considering the high silicon doping and the presence of Ga vacancies, we attribute the observed state primarily to Si-related defects.

Selenium vacancies have previously been associated with acceptor levels in bulk GaSe at approximately 0.5 eV below the CBM^{55,56}. Our calculations place V_{Se} at 0.41 eV below the CBM, overlapping with the energy range of the silicon-related

defects. However, given the high Si concentration in our samples with Si_{Se} exhibiting a formation energy comparable to V_{Se} and the low formation energy of the electronically inactive O_{Se} (see Figures S4-S8 in the Supplementary Information), we exclude V_{Se} as the dominant defect species. This interpretation is consistent with previous structural studies on atomically thin GaSe , which reported the observation of both Se vacancies and O substituting Se⁵⁴. Also note that the oxidation of V_{Se} appears to be the primary process driving the degradation of GaSe under dark conditions⁵⁷.

The defect observed in both DLOS and SSPC spectroscopy, approximately 1.8 eV below the CBM, is consistent with the calculated energy levels of an O-passivated Ga vacancy O_{Ga} or Se_{Ga} . The former would be in line with the high oxygen content and the presence of Ga vacancies. However, the formation energy for O_{Ga} is much higher than Se_{Ga} , making it less probable to form. A definitive distinction could be achieved by correlating the DLOS signal with controlled oxygen exposure, which lies beyond the scope of the present work and is left for future studies. In addition to these point defects, extended defects, such as trigonal defects and metallic inclusions, have been reported in GaSe ^{54,58}. While we cannot exclude the presence of large traps, the wide variation in size would lead to a correspondingly broad distribution of defect energetic positions and capture cross-sections. Finally, the observed Urbach tails at the band edges indicate the presence of shallow, distributed defect states. These are typically associated with defect continua arising from interfacial defects, dielectric defects, or extended defects within the GaSe layers, and their identification is correspondingly more challenging. A comprehensive analysis of these defects is left for future studies.

IV. CONCLUSIONS

In this study, we systematically investigated the defect landscape of few-layer silicon-doped GaSe using a combination of electrical, optical, and temperature-dependent spectroscopies, which reveal defect energies and capture cross-sections consistent with DFT calculations and previous reports. Using these complementary techniques, we identify multiple electrically active defects in silicon-doped GaSe . Specifically, we observe 4 acceptors: three deep levels located at approximately 0.88 eV (Si_{Se}), 1.4 eV (Ga_{Se} , cross-technique average), and 1.8 eV ($\text{O}_{\text{Ga}}/\text{Se}_{\text{Ga}}$, cross-technique average) below the CBM, and one acceptor at ~ 0.16 eV above the VBM, attributed to V_{Ga} . In addition, we identify a donor state at ~ 0.25 eV (cross-technique average) below the CBM, consistent with Si_{Ga} . Our results highlight the critical role of silicon in creating states inside the bandgap and suggest that gallium vacancies remain one of the dominant electrically active defects.

These findings underline the importance of controlling defect chemistry in 2D- GaSe to tailor its electronic properties for next-generation devices. Looking ahead, as scalable, large-area epitaxy of van der Waals PTMCs becomes mature⁵⁹⁻⁶² and device architectures continue to be refined^{63,64}, defect

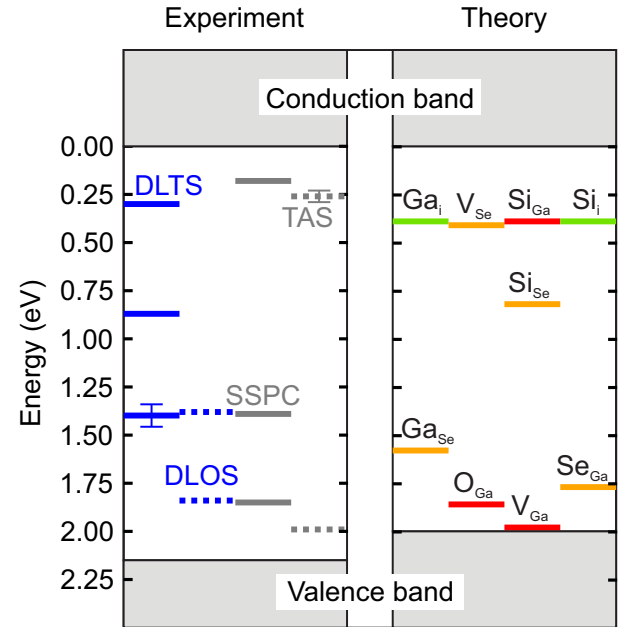


FIG. 4. Comparison between experimentally measured (left) and DFT-calculated (right) mid-gap states and band-edge positions relative to the CBM. Left: Deep levels detected experimentally by DLTS (continuous blue), DLOS (dotted blue), SSPC (continuous gray), and TAS (dotted gray). Right: Defect levels for various point defects calculated by DFT. The colour of each marker indicates the defect site: green for interstitial positions, yellow for selenium sites, and red for gallium sites. Solid black lines indicate the CBM and VBM.

control will be a determining factor in achieving reproducible electronic and optoelectronic performance. In this context, the integration of complementary characterization techniques, as demonstrated here, provides a robust framework for systematic optimization of PTMC material properties and represents an essential step toward integration-ready 2D materials technologies.

V. EXPERIMENTAL SECTION

A. Crystal growth

GaSe bulk crystals were prepared by direct reaction from elements in a quartz ampoule. Gallium (99.9999%, Wuhan Xinrong New Materials Co., China) and selenium (2–4 mm, 99.9999%, Wuhan Xinrong New Materials Co., China) corresponding to 25 g of GaSe were placed in a quartz ampoule (25 × 100 mm, quartz purity over 99.99%) and melt sealed with an oxygen–hydrogen welding torch under high vacuum ($< 1 \times 10^{-3}$ Pa using an oil diffusion pump with LN_2 cold trap). The ampoule was placed in a muffle furnace and heated to 900 °C using a heating rate of 1 °C/min. After 5 hours at that temperature, the furnace was cooled to 500 °C using a cooling rate of 5 °C/hour and finally freely cooled to room temperature. The ampoule was opened in an argon-filled glovebox.

B. Sample Fabrication

The few-layer flake (7.1 nm thick, corresponding to \sim 8 monolayers; see Figure S9 in the Supplementary Information) of gallium selenide was mechanically exfoliated from bulk crystals. The flake was electrically contacted using a few-layer graphite electrode and subsequently transferred onto a c-plane sapphire substrate. To protect the sample from oxidation, a hexagonal boron nitride (hBN) encapsulation layer was used, which also served as the gate dielectric. A 7 nm platinum (Pt) layer was then evaporated onto the top surface to serve as a transparent top electrode.

C. Impedance and Optical Measurements

Capacitance-voltage (CV) curves and transient signals were recorded using a Zurich Instruments MFIA Impedance Analyzer, capable of measuring capacitance across frequencies from 1 mHz to 5 MHz and on time scales as short as 10 μ s. The samples were mounted on a sample holder in direct contact with the cryostat cold finger to ensure stable thermal conditions. Optical excitation was provided by a NKT Photonics SuperK Fianium laser coupled with a VIS HP8 tunable bandpass filter, offering continuous wavelength tuning from 400 nm to 1000 nm (<2.5 meV bandwidth). Temperature- and time-dependent capacitance measurements were conducted over the range of 75 K to 300 K, with a temperature precision of \pm 500 mK. Photocapacitance data were acquired at 20 K using monochromatic light with wavelengths ranging from 400 nm to 1000 nm.

D. Theoretical Methods

Density functional theory (DFT) ab-initio calculations were employed to identify defects observed via DLTS. Calculations were performed using the Vienna Ab initio Simulation Package (VASP)⁶⁵ with the projector augmented wave method⁶⁶. The cutoff for wave-function expansion was 400 eV. We took van der Waals interactions into account by the Tkatchenko-Scheffler method⁶⁷. Defect states were modelled in a supercell with lattice vectors (4a, 2a+4b, c), where a, b and c are the primitive unit vectors. We took a 2 x 2 x 2 Γ -centered k-point set. The structure optimization was performed with the exchange-correlation energy functional by Perdew, Burke and Ernzerhof⁶⁸ and the total energy calculations were carried out by use of a HSE hybrid functional⁶⁹ with the fraction of exact exchange 0.3. Total energy of charged system was corrected by the SLABCC code⁷⁰. The formation energy was evaluated following the method in Ref.⁷¹. The equilibrium position of Ga_i is between two layers and, on the other hand, Se_i occupies a puckered bond-center interstitial site between a pair of Ga atoms. In the system with V_{Ga}, the pair of the missing Ga atom moves toward the middle of the layer. For other defects, only small rearrangements of the neighboring atoms were seen. These positions are consistent with other

calculations⁴⁵. Si_i and O_i also occupy a puckered bond-center interstitial site between a Ga pair.

SUPPORTING INFORMATION

Supporting Information is available from the ...Online Library or from the author.

ACKNOWLEDGMENTS

The work was partly funded by the German Research Foundation (DFG) under Germany's Excellence Strategy via the Clusters of Excellence e-conversion (EXC-2089/1-390776260) and the MCQST (EXC-2111-390814868) and via Grants FI 947/7-1, FI 947/8-1 and KO4005-9/1. Z.S. was supported by the ERC-CZ program (project LL2101) from the Ministry of Education, Youth and Sports (MEYS) and by the project Advanced Functional Nanorobots (reg. No. CZ.02.1.01/0.0/0.0/15_003/0000444 financed by the EFRR). Z.S. acknowledges the assistance provided by the Advanced Multiscale Materials for Key Enabling Technologies project, supported by the Ministry of Education Youth, and Sports of the Czech Republic. Project No. CZ.02.01.01/00/22_008/0004558, co-funded by the European Union.

CONFLICT OF INTEREST

The authors declare no conflict of interest

DATA AVAILABILITY STATEMENT

The data that support the findings of this study are available from the corresponding author upon reasonable request.

¹J. Hong, C. Jin, J. Yuan, and Z. Zhang, "Atomic defects in two-dimensional materials: From single-atom spectroscopy to functionalities in opto-/electronics, nanomagnetism, and catalysis," *Advanced Materials* **29**, 1606434 (2017).

²J. Xiong, J. Di, J. Xia, W. Zhu, and H. Li, "Surface defect engineering in 2d nanomaterials for photocatalysis," *Advanced Functional Materials* **28**, 1801983 (2018).

³X. Liu and M. C. Hersam, "2d materials for quantum information science," *Nature Reviews Materials* **4**, 669–684 (2019).

⁴A. Carbone, D.-P. Bendixen-Fernex de Mongex, A. V. Krasheninnikov, M. Wubs, A. Huck, T. W. Hansen, A. W. Holleitner, N. Stenger, and C. Kastl, "Creation and microscopic origins of single-photon emitters in transition-metal dichalcogenides and hexagonal boron nitride," *Applied Physics Reviews* **12**, 031333 (2025).

⁵H. Cai, Y. Gu, Y.-C. Lin, Y. Yu, D. B. Geohegan, and K. Xiao, "Synthesis and emerging properties of 2D layered III–VI metal chalcogenides," *Applied Physics Reviews* **6**, 041312 (2019).

⁶M. Yu, M. Hilse, Q. Zhang, Y. Liu, Z. Wang, and S. Law, "Review of Nanolayered Post-transition Metal Monochalcogenides: Synthesis, Properties, and Applications," *ACS Applied Nano Materials*, acsanm.3c05984 (2024).

⁷Z. Wang, M. Safdar, M. Mirza, K. Xu, Q. Wang, Y. Huang, F. Wang, X. Zhan, and J. He, "High-performance flexible photodetectors based on GaTe nanosheets," *Nanoscale* **7**, 7252–7258 (2015).

⁸S. Sorifi, M. Moun, S. Kaushik, and R. Singh, "High-temperature performance of a gase nanosheet-based broadband photodetector," *ACS Applied Electronic Materials* **2**, 670–676 (2020).

⁹E. G. Demissie and C.-K. Siu, "Theoretical understanding of the structure–property relationship of oxygen-doped gallium selenide as an efficient photocatalyst for oxygen evolution reaction," *The Journal of Physical Chemistry C* **128**, 10397–10406 (2024).

¹⁰M.-W. Chen, H. Kim, D. Ovchinnikov, A. Kuc, T. Heine, O. Renault, and A. Kis, "Large-grain MBE-grown GaSe on GaAs with a Mexican hat-like valence band dispersion," *npj 2D Materials and Applications* **2**, 2 (2018).

¹¹A. Budweg, D. Yadav, A. Grupp, A. Leitenstorfer, M. Trushin, F. Pauly, and D. Brida, "Control of excitonic absorption by thickness variation in few-layer gase," *Phys. Rev. B* **100**, 045404 (2019).

¹²D. V. Rybkovskiy, A. V. Osadchy, and E. D. Obraztsova, "Transition from parabolic to ring-shaped valence band maximum in few-layer gas, gase, and inse," *Phys. Rev. B* **90**, 235302 (2014).

¹³T. Cao, Z. Li, and S. G. Louie, "Tunable magnetism and half-metallicity in hole-doped monolayer gase," *Phys. Rev. Lett.* **114**, 236602 (2015).

¹⁴D. Wickramaratne, F. Zahid, and R. K. Lake, "Electronic and thermoelectric properties of van der waals materials with ring-shaped valence bands," *Journal of Applied Physics* **118**, 075101 (2015).

¹⁵Z. Xu, Q. Xia, L. Zhang, and G. Gao, "A van der waals p–n heterostructure of gase/sns2: a high thermoelectric figure of merit and strong anisotropy," *Nanoscale* **16**, 2513–2521 (2024).

¹⁶D. Leykam, S. Flach, O. Bahat-Treidel, and A. S. Desyatnikov, "Flat band states: Disorder and nonlinearity," *Phys. Rev. B* **88**, 224203 (2013).

¹⁷P. Das, D. Wickramaratne, B. Debnath, G. Yin, and R. K. Lake, "Charged impurity scattering in two-dimensional materials with ring-shaped valence bands: Gas, gase, ins, and inse," *Phys. Rev. B* **99**, 085409 (2019).

¹⁸J. H. Neave, P. J. Dobson, J. J. Harris, P. Dawson, and B. A. Joyce, "Silicon doping of mbe-grown gaas films," *Applied Physics A* **32**, 195–200 (1983).

¹⁹M. Suezawa, A. Kasuya, Y. Nishina, and K. Sumino, "Optical studies of heat-treated si-doped gaas bulk crystals," *Journal of Applied Physics* **69**, 1618–1624 (1991).

²⁰C. Domke, P. Ebert, M. Heinrich, and K. Urban, "Microscopic identification of the compensation mechanisms in si-doped gaas," *Phys. Rev. B* **54**, 10288–10291 (1996).

²¹D. Ruhstorfer, S. Mejia, M. Ramsteiner, M. Döblinger, H. Riedl, J. J. Finley, and G. Koblmüller, "Demonstration of n-type behavior in catalyst-free si-doped gaas nanowires grown by molecular beam epitaxy," *Applied Physics Letters* **116**, 052101 (2020).

²²J. Klein, M. Lorke, M. Florian, F. Sigger, L. Sigl, S. Rey, J. Wierzbowski, J. Cerne, K. Müller, E. Mitterreiter, P. Zimmermann, T. Taniguchi, K. Watanabe, U. Wurstbauer, M. Kaniber, M. Knap, R. Schmidt, J. J. Finley, and A. W. Holleitner, "Site-selectively generated photon emitters in monolayer mos2 via local helium ion irradiation," *Nature Communications* **10**, 2755 (2019).

²³L. G. Cançado, A. Jorio, E. H. M. Ferreira, F. Stavale, C. A. Achete, R. B. Capaz, M. V. O. Moutinho, A. Lombardo, T. S. Kulmala, and A. C. Ferrari, "Quantifying defects in graphene via raman spectroscopy at different excitation energies," *Nano Letters* **11**, 3190–3196 (2011).

²⁴T. Grüneitner, A. Henning, M. Bissolo, M. Zengerle, L. Gregoratti, M. Amati, P. Zeller, J. Eichhorn, A. V. Stier, A. W. Holleitner, J. J. Finley, and I. D. Sharp, "Real-time investigation of sulfur vacancy generation and passivation in monolayer molybdenum disulfide via in situ x-ray photoelectron spectromicroscopy," *ACS Nano* **16**, 20364–20375 (2022).

²⁵T. Ohta, A. Klust, J. A. Adams, Q. Yu, M. A. Olmstead, and F. S. Ohuchi, "Atomic structures of defects at gase/si(111) heterointerfaces studied by scanning tunneling microscopy," *Phys. Rev. B* **69**, 125322 (2004).

²⁶W. Zhou, X. Zou, S. Najmaei, Z. Liu, Y. Shi, J. Kong, J. Lou, P. M. Ajayan, B. I. Yakobson, and J.-C. Idrobo, "Intrinsic structural defects in monolayer molybdenum disulfide," *Nano Letters* **13**, 2615–2622 (2013).

²⁷P. Ci, X. Tian, J. Kang, A. Salazar, K. Eriguchi, S. Warkander, K. Tang, J. Liu, Y. Chen, S. Tongay, W. Walukiewicz, J. Miao, O. Dubon, and J. Wu, "Chemical trends of deep levels in van der waals semiconductors," *Nature Communications* **11** (2020), 10.1038/s41467-020-19247-1.

²⁸Y. Zhao, M. Tripathi, K. Černevičs, A. Avsar, H. G. Ji, J. F. Gonzalez Marin, C.-Y. Cheon, Z. Wang, O. V. Yazyev, and A. Kis, "Electrical spectroscopy of defect states and their hybridization in monolayer mos2," *Nature Communications* **14** (2023), 10.1038/s41467-022-35651-1.

²⁹H. Ghadi, J. F. McGlone, Z. Feng, A. F. M. A. U. Bhuiyan, H. Zhao, A. R. Arehart, and S. A. Ringel, "Influence of growth temperature on defect states throughout the bandgap of mocvd-grown β -ga2o3," *Applied Physics Letters* **117** (2020), 10.1063/5.0025970.

³⁰P. Kruszewski, K. Sakowski, K. Gościński, and P. Prystawko, "The photoionization processes of deep trap levels in n-gan films grown by movpe technique on ammono-gan substrates," *Applied Sciences* **14** (2024), 10.3390/app14198785.

³¹T. Knobloch, Y. Illarionov, F. Ducry, C. Schleich, S. Wachter, K. Watanabe, T. Taniguchi, T. Mueller, M. Waltl, M. Lanza, M. Vexler, M. Luisier, and T. Grasser, "The performance limits of hexagonal boron nitride as an insulator for scaled cmos devices based on two-dimensional materials," *Nature Electronics* **4**, 98–108 (2021).

³²A. Kurtz, E. Muñoz, J. M. Chauveau, and A. Hierro, "Deep-level spectroscopy in metal–insulator–semiconductor structures," *Journal of Physics D: Applied Physics* **50**, 065104 (2017).

³³S. Shigetomi and T. Ikari, "Impurity effect on electrical conduction in n-gase doped with si, sn and ge," *Japanese Journal of Applied Physics* **44**, 7521– (2005).

³⁴D. V. Lang, "Deep-level transient spectroscopy: A new method to characterize traps in semiconductors," *Journal of Applied Physics* **45**, 3023–3032 (1974).

³⁵E. Mooser and M. Schlüter, "The band-gap excitons in gallium selenide," *Il Nuovo Cimento B* (1971–1996) **18**, 164–208 (1973).

³⁶G. Ottaviani, C. Canali, F. Nava, P. Schmid, E. Mooser, R. Minder, and I. Zschokke, "Gase: A layer compound with anomalous valence band anisotropy," *Solid State Communications* **14**, 933–936 (1974).

³⁷G. Lucovsky, "On the photoionization of deep impurity centers in semiconductors," *Solid State Communications* **3**, 299–302 (1965).

³⁸N. Fernelius, "Properties of gallium selenide single crystal," *Progress in Crystal Growth and Characterization of Materials* **28**, 275–353 (1994).

³⁹S. G. Choi, D. H. Levi, C. Martinez-Tomas, and V. Muñoz Sanjosé, "Above-bandgap ordinary optical properties of gase single crystal," *Journal of Applied Physics* **106**, 053517 (2009).

⁴⁰A. Gaur, D. Chiappe, D. Lin, D. Cott, I. Asselberghs, M. Heyns, and I. Radu, "Analysis of admittance measurements of mos capacitors on cvd grown bilayer mos2," *2D Materials* **6**, 035035 (2019).

⁴¹S. Sze and K. K. Ng, "Physics of semiconductor devices," (2006).

⁴²D. K. Schroder, "Semiconductor material and device characterization," (2005).

⁴³R. Schifano, E. Monakhov, B. Svensson, W. Mtangi, P. Janse van Rensburg, and F. Auret, "Shallow levels in virgin hydrothermally grown n-type zno studied by thermal admittance spectroscopy," *Physica B: Condensed Matter* **404**, 4344–4348 (2009).

⁴⁴Z. Ben Aziza, V. Zólyomi, H. Henck, D. Pierucci, M. G. Silly, J. Avila, S. J. Magorrian, J. Chaste, C. Chen, M. Yoon, K. Xiao, F. Sirotti, M. C. Asensio, E. Lhuillier, M. Eddrief, V. I. Fal'ko, and A. Ouerghi, "Valence band inversion and spin-orbit effects in the electronic structure of monolayer gase," *Phys. Rev. B* **98**, 115405 (2018).

⁴⁵P. Deák, M. Han, M. Lorke, M. F. Tabriz, and T. Frauenheim, "Intrinsic defects of gase," *Journal of Physics: Condensed Matter* **32**, 285503 (2020).

⁴⁶C. Manfredotti, R. Murri, A. Quirini, and L. Vasanelli, "Photoelectronic properties of n-gase," *physica status solidi (a)* **38**, 685–693 (1976).

⁴⁷V. Capozzi and A. Minafra, "Photoluminescence properties of cu-doped gase," *Journal of Physics C: Solid State Physics* **14**, 4335 (1981).

⁴⁸V. Capozzi, "Kinetics of radiative recombinations in gase and influence of cu doping on the luminescence spectra," *Phys. Rev. B* **28**, 4620–4627 (1983).

⁴⁹V. Capozzi and M. Montagna, "Optical spectroscopy of extrinsic recombinations in gallium selenide," *Phys. Rev. B* **40**, 3182–3190 (1989).

⁵⁰Y. Cui, R. Dupere, A. Burger, D. Johnstone, K. C. Mandal, and S. A. Payne, "Acceptor levels in gase:in crystals investigated by deep-level transient spectroscopy and photoluminescence," *Journal of Applied Physics* **103**, 013710 (2008).

⁵¹M. K. Anis and A. R. Piercy, "Electrical conduction in p-gase," *Journal of Physics D: Applied Physics* **17**, 1229 (1984).

⁵²R. A. Redkin, N. I. Onishchenko, A. V. Kosobutsky, V. N. Brudnyi, X. Su, and S. Y. Sarkisov, "Temperature-dependent optical absorption and dlts study of as-grown and electron-irradiated gase crystals," *Crystals* **15** (2025), 10.3390/cryst15040372.

⁵³G. Micocci, P. Siciliano, and A. Tepore, "Deep level spectroscopy in p-gase single crystals," *Journal of Applied Physics* **67**, 6581–6582 (1990).

⁵⁴D. G. Hopkinson, V. Zólyomi, A. P. Rooney, N. Clark, D. J. Terry, M. Hamer, D. J. Lewis, C. S. Allen, A. I. Kirkland, Y. Andreev, Z. Kudrynskyi, Z. Kovalyuk, A. Patanè, V. I. Fal'ko, R. Gorbachev, and S. J. Haigh, "Formation and healing of defects in atomically thin gase and inse," *ACS Nano* **13**, 5112–5123 (2019).

⁵⁵G. Micocci, A. Serra, and A. Tepore, "Impurity levels in sn-doped gase semiconductor," *physica status solidi (a)* **162**, 649–659 (1997).

⁵⁶S. Shigetomi and T. Ikari, "Optical and electrical properties of p-gase doped with in," *Japanese Journal of Applied Physics* **46**, 5774 (2007).

⁵⁷L. Shi, Q. Li, Y. Ouyang, and J. Wang, "Effect of illumination and se vacancies on fast oxidation of ultrathin gallium selenide," *Nanoscale* **10**, 12180–12186 (2018).

⁵⁸P. Tonndorf, S. Schwarz, J. Kern, I. Niehues, O. Del Pozo-Zamudio, A. I. Dmitriev, A. P. Bakhtinov, D. N. Borisenko, N. N. Kolesnikov, A. I. Taratkovskii, S. Michaelis de Vasconcellos, and R. Bratschitsch, "Single-photon emitters in gase," *2D Materials* **4**, 021010 (2017).

⁵⁹E. Zallo, A. Pianetti, A. S. Prikhodko, S. Cecchi, Y. S. Zaytseva, A. Giuliani, M. Kremser, N. I. Borgardt, J. J. Finley, F. Arciprete, M. Palummo, O. Pulci, and R. Calarco, "Two-dimensional single crystal monoclinic gallium telluride on silicon substrate via transformation of epitaxial hexagonal phase," *npj 2D Materials and Applications* **7**, 19 (2023).

⁶⁰M. Bissolo, M. Hanke, R. Calarco, J. J. Finley, G. Koblmüller, J. M. J. Lopes, and E. Zallo, "Van der waals epitaxy of 2d gallium telluride on graphene: Growth dynamics and principal component analysis," *Small* (2025), 10.1002/smll.202503993.

⁶¹M. Bissolo, M. Dembecki, J. Belz, J. Schabesberger, M. Bergmann, P. Avdienko, F. Rauscher, A. S. Ulhe, H. Riedl, K. Volz, J. J. Finley, E. Zallo, and G. Koblmüller, "Unveiling the growth mode diagram of gase on sapphire," *Communications Materials* **6**, 279 (2025).

⁶²A. Pianetti, S. Cecchi, M. Hanke, J. J. Finley, F. Arciprete, R. Calarco, and E. Zallo, "Epitaxy and phase stability of 2d hexagonal gallium telluride on silicon," *physica status solidi (RRL) – Rapid Research Letters* **n/a**, e202500432 (2025).

⁶³Z. Liu, J. Wang, B. Chen, Y. Wei, W. Liu, and J. Liu, "Giant enhancement of continuous wave second harmonic generation from few-layer gase coupled to high-q quasi bound states in the continuum," *Nano Letters* **21**, 7405–7410 (2021).

⁶⁴C. Xue, C. Tan, X. Gao, J. Tang, W. Sun, Y. Yin, M. Wang, X. Gao, H. An, B. Fu, W. Liu, Y. Wang, Y. Li, F. Ding, and H. Peng, "Wafer-scale uniform epitaxy of transferable 2d single crystals for gate-all-around nanosheet field effect transistors," *Nature Communications* **16** (2025), 10.1038/s41467-025-65641-y.

⁶⁵G. Kresse and J. Furthmüller, "Efficient iterative schemes for ab initio total-energy calculations using a plane-wave basis set," *Phys. Rev. B* **54**, 11169–11186 (1996).

⁶⁶G. Kresse and D. Joubert, "From ultrasoft pseudopotentials to the projector augmented-wave method," *Phys. Rev. B* **59**, 1758–1775 (1999).

⁶⁷A. Tkatchenko and M. Scheffler, "Accurate molecular van der waals interactions from ground-state electron density and free-atom reference data," *Phys. Rev. Lett.* **102**, 073005 (2009).

⁶⁸J. P. Perdew, K. Burke, and M. Ernzerhof, "Generalized gradient approximation made simple," *Phys. Rev. Lett.* **77**, 3865–3868 (1996).

⁶⁹A. V. Kruckau, O. A. Vydrov, A. F. Izmaylov, and G. E. Scuseria, "Influence of the exchange screening parameter on the performance of screened hybrid functionals," *The Journal of Chemical Physics* **125**, 224106 (2006).

⁷⁰M. Farzalipour Tabriz, B. Aradi, T. Frauenheim, and P. Deák, "Slabcc: Total energy correction code for charged periodic slab models," *Computer Physics Communications* **240**, 101–105 (2019).

⁷¹C. Freysoldt, B. Grabowski, T. Hickel, J. Neugebauer, G. Kresse, A. Janotti, and C. G. Van de Walle, "First-principles calculations for point defects in solids," *Rev. Mod. Phys.* **86**, 253–305 (2014).